electronics

Article

FPGA-Based Implementation of an Adaptive Noise Controller for Continuous Wave Superconducting Cavity

Fatemeh Abdi [1,*], Wojciech Cichalewski [1], Wojciech Jałmużna [1], Łukasz Butkowski [2], Julien Branlard [2], Andrea Bellandi [2] and Grzegorz Jabłoński [1]

[1] Department of Microelectronics and Computer Science, Łódź University of Technology, 93-005 Łódź, Poland; wojciech.cichalewski@p.lodz.pl (W.C.); wojciech.jalmuzna@p.lodz.pl (W.J.)
[2] Deutsches Elektronen-Synchrotron DESY, Notkestr. 85, 22607 Hamburg, Germany; lukasz.butkowski@desy.de (Ł.B.); julien.branlard@desy.de (J.B.); andrea.bellandi@desy.de (A.B.)
* Correspondence: fatemeh.abdi@dokt.p.lodz.pl

Abstract: Low-level radio frequency (LLRF) systems have been designed to regulate the accelerator field in the cavity; these systems have been used in the free electron laser (FLASH) and European X-ray free-electron laser (E-XFEL). However, the reliable operation of these cavities is often hindered by two primary sources of noise and disturbances: Lorentz force detuning (LFD) and mechanical vibrations, commonly known as microphonics. This article presents an innovative solution in the form of a narrowband active noise controller (NANC) designed to compensate for the narrowband mechanical noise generated by certain supporting machines, such as vacuum pumps and helium pressure vibrations. To identify the adaptive filter coefficients in the NANC method, a least mean squares (LMS) algorithm is put forward. Furthermore, a variable step size (VSS) method is proposed to estimate the adaptive filter coefficients based on changes in microphonics, ultimately compensating for their effects on the cryomodule. An accelerometer with an SPI interface and some transmission boards are manufactured and mounted at the cryomodule test bench (CMTB) to measure the microphonics and transfer them via Ethernet cable from the cryomodule side to the LLRF crate side. Several locations had been selected to find the optimal location for installing the accelerometer. The proposed NANC method is characterized by low computational complexity, stability, and high tracking ability. By addressing the challenges associated with noise and disturbances in cavity operation, this research contributes to the enhanced performance and reliability of LLRF systems in particle accelerators.

Keywords: narrowband active noise controller (NANC); least mean squares (LMS); field-programmable gate array (FPGA); microphonics; accelerator; continuous wave (CW)

Citation: Abdi, F.; Cichalewski, W.; Jałmużna, W.; Butkowski, Ł.; Branlard, J.; Bellandi, A.; Jabłoński, G. FPGA-Based Implementation of an Adaptive Noise Controller for Continuous Wave Superconducting Cavity. *Electronics* **2024**, *13*, 155. https://doi.org/10.3390/electronics13010155

Academic Editor: Akash Kumar

Received: 25 November 2023
Revised: 23 December 2023
Accepted: 27 December 2023
Published: 29 December 2023

1. Introduction

Currently, the free electron laser in Hamburg (FLASH) [1] and the European X-ray free-electron laser (E-XFEL) utilize a digital low-level radio frequency (LLRF) control system based on field-programmable gate array (FPGA) technology to stabilize the accelerator field at facilities [2]. FPGA technology is employed in the control system design to maximize computation power while minimizing latency.

In particle accelerator facilities, two distinct operational modes are used: pulsed or continuous wave (CW). The maximum number of particle bunches that a particle accelerator can create in pulsed mode is typically in the range of a few ten thousand bunches per second; however, the beam energy can be quite high (17.5 GeV for the E-XFEL). Short pulses require MHz beam injection, and the duty cycle is relatively low because the accelerator operates in bursts with significant downtime between bunch trains.

CW accelerators operate with a steady stream of particle bunches, often at a significantly lower frequency than pulsed accelerators, but yield a higher number of bunches per second (up to a million). On the other hand, the CW mode typically has lower energy than the pulsed mode (4–8 GeV). For these reasons, research and development (R&D) programs focused on the potential upgrade of the E-XFEL for CW operations are of high interest. The steady and effectively higher bunch throughput is the main motivation for users to explore CW machines with simplified beam detection and diagnostic systems [3,4].

The application of the conventional proportional-integral (PI) control method for resonance control feedback in the cavities is restricted by the mechanical properties of the cavities. The transfer function of the actuators, when considered in conjunction with the cavity, exhibits poles in a frequency range proximate to the prevailing components of microphonic disturbances. Consequently, the use of the PI control scheme proves ineffective due to an inadequate phase margin within the crossover frequency range. To surmount these limitations, more sophisticated algorithms have been devised and implemented, such as the active noise controller (ANC) and narrowband active noise controller (NANC) methods. Both the ANC and the NANC methods are commonly employed to reduce noise in many media, and these techniques have also been applied to superconducting radio frequency cavities [5]. Mechanical vibrations (microphonics) are generated in the accelerator environment by various sources, like vacuum pumps, helium pressure vibrations, and fans. Microphonics change the mechanical dimensions of the cavities, which results in a shift in the resonant frequency. To counteract this, the accelerating structure must be tuned to the specified resonance frequency. The detuning frequency, the difference between the actual frequency and the resonance frequency, should be cancelled using an advanced controller [6,7].

According to measurements made at the cryomodule test bench (CMTB), the microphonics are frequencies below 500 Hz that change based on the characteristics, size, and placement of the cavity concerning its surroundings [8]. The ANC controller was implemented for microphonics effects at CMTB. This controller, however, has a longer response time and concentrates on the detuning determined from the RF signal, while the operators must manually set the microphonics frequency and the step size of the ANC method.

In this paper, we propose an advanced NANC method to control and track microphonic disturbances. This controller utilizes the variable step-size least mean squares (VSS LMS) algorithm to identify and estimate the adaptive filter coefficients based on the microphonics changes. The controller produces a signal with the same amplitude and opposite phase of the microphonic disturbances. The step-size parameter significantly influences the LMS algorithm's performance. Initially, a large step size is necessary to quickly adapt to the noise changes. A smaller step size ensures minimal misadjustment and stability after the error signal converges to a minimum value [9].

2. Controller Loops

The LLRF System Comprises Two Control Loops

Using 16-b analog-to-digital converters, RF signals (1.3 GHz) are first down-converted to 54.17 MHz and then sampled at 81.25 MHz. After that, the in-phase (I) and quadrature (Q) signals are made available for control signal production by using the non-I/Q detection algorithm. The DRTM-DWC10 rear transition module and the SIS8300L advanced mezzanine card combination are used for down-conversion and I/Q detection. To handle the forward, reflected, and pick-up signals from the cavities, three RTM-AMC pairs are required. The detector board computes the vs. signal (2×18 b). After that, it is transmitted over the MicroTCA.4 backplane to the DAMC-TCK7B controller. A 3.2-Gb serial connection using a low-latency proprietary protocol is used for this purpose.

1. The LLRF controller is responsible for stabilizing the accelerator field. Figure 1 provides an overview of the LLRF control system currently in operation at CMTB.
2. The primary LLRF controller algorithms are implemented on a dedicated data processing card. The LLRF controller's output is then transmitted to an upconverter/vector modulator card, and the resulting signals drive the preamplifier and inductive output tube (IoT) [10,11].
3. The detuning controller loop aims to stabilize the resonance frequency of the cavities.

4. This paper primarily focuses on the implementation of the detuning controller. An approach has been proposed to identify microphonics changes and estimate adaptive filter coefficients using the VSS LMS algorithm.

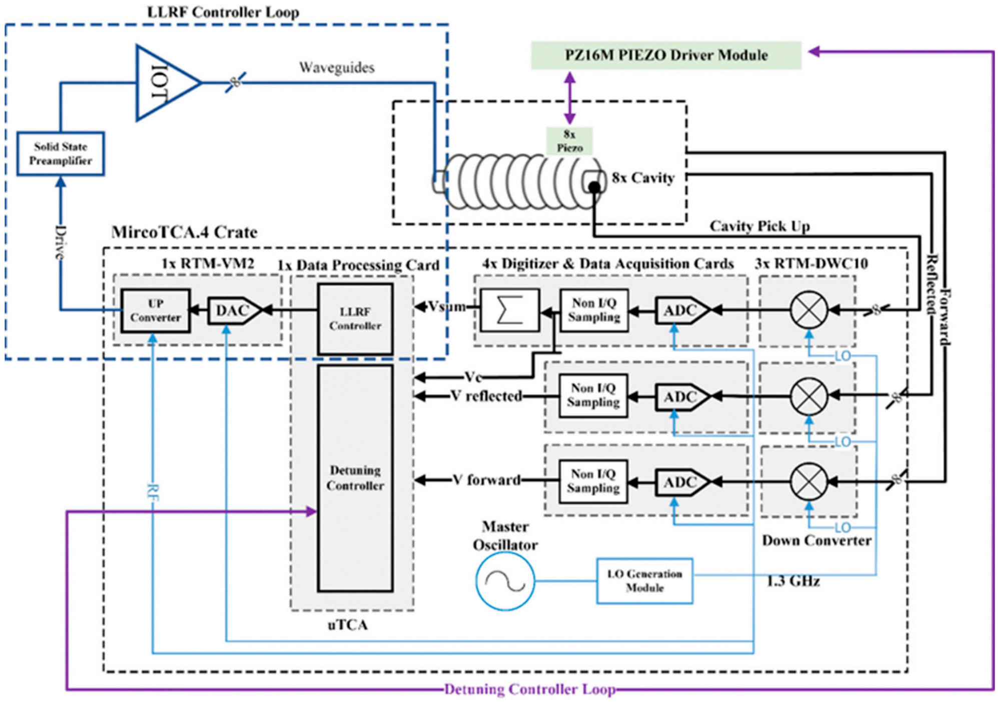

Figure 1. A general view of the LLRF control system at CMTB.

3. Compensation Method for Microphonics Detuning

The noise sources and resulting noise signals are frequently periodic in ANC applications. These periodic noise signals are produced by rotating machinery like motors, fans, compressors, and engines. Since sine waves have fundamental and harmonic components, each periodic signal can be expanded as the sum of several sine waves by using the Fourier series theory.

The noise source's basic frequency is picked up by a sensor or an accelerometer. A signal generator uses this data to produce a periodic signal with the same source's fundamental frequency. The generated signal is sent via an adaptive filter (the ANC filter), which modifies its spectrum to match the noise at the canceling loudspeaker's amplitude and phase (with the opposite sign). The error signal detects unwanted noise and gives instructions for ANC filter adaptation.

Mechanical noises, generated by vacuum pumps, compressors, refrigeration equipment, helium boiling, and turbulent flows in pipes, are typically periodic [12].

An advanced narrowband active noise controller (NANC) method is proposed to compensate for the mechanical noise. It provides a reference signal that includes the fundamental frequency and all harmonics of the mechanical noise. In the NANC method, two types of reference signals are commonly used:

1. An impulse train with a period equal to the inverse of the fundamental frequency of the periodic noise [13,14].
2. Sinewaves that match the frequencies of the corresponding harmonic tones are to be cancelled. A particular sinusoid signal can be eliminated by a finite impulse response (FIR) notch filter in the NANC method while having very little impact on narrowband noise, as shown in Figure 2. The second technique, the adaptive FIR notch filter, was developed to cancel tonal interference [15] and has been adapted for use in the periodic NANC method [16].

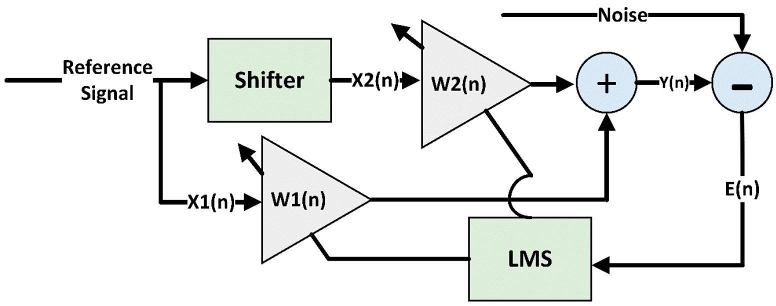

Figure 2. Single-frequency adaptive FIR notch filter.

The proposed NANC method is implemented using an adaptive FIR notch filter, offering the advantages of easy bandwidth control and precise frequency tracking of the mechanical noise. Within the adaptive notch filter, two adaptive coefficients are used: $x_1(n) = A \times \sin(w_0 n)$ and $x_2(n) = A \times \cos(w_0 n)$. These are individually weighted and then summed to produce the controller's output signal (Y(n)). The LMS algorithm is employed to update the filter coefficients ($w_1(n)$ and $w_2(n)$) and minimize the residual error (E(n)). According to Figure 2, an error signal is the difference between the noise and the controller's output signal.

The NANC method, incorporating the VSS LMS algorithm implemented with hardware description language (HDL), is utilized to adapt to changes in the resonance frequency of the cavity induced by microphonics. This is especially important for perturbations in the narrow band when the disturbance can be represented as the sum of sine waves. The ANC's parameters can be adjusted in general while the system is operating by iteratively optimizing the filter coefficients that are implemented in the high-level software. Complementing existing research in LLRF, the NANC with VSSLMS algorithm offers novel insights and advancements in control precision. Supplementing the related work in LLRF, the NANC system, driven by the VSSLMS algorithm, introduces innovative approaches for improved performance and stability.

Narrowband Active Noise Controller Components

The algorithms are inherently susceptible to measurement noise because the magnitude of the estimation error determines the step size. The algorithm is robust to low signal-to-noise ratio environments and has a lower computing complexity due to the application of the sign-based criterion in the step-size estimation procedure. By reducing rounding error, the suggested structure optimizes the fixed-point implementation and permits a reduction in the word length. As depicted in Figure 3, the presented method comprises four components:

The first component, the adaptive filter component, implements the adaptive FIR notch filter. Its purpose is to generate the controller output, which contains the same amplitude and opposite phase as the microphonics signal. The FIR notch filter is implemented to calculate the controller output signal based on Equation (1) and transfer it to the actuator. Input signals should be multiplied by $w_{1,i,x}(n)$ and $w_{2,i,x}(n)$ (filter coefficients), respectively [17]. Some dual-port memories (DPM) are used to store the frequency, coefficients, and step size, and the D block is a D flip-flop for shifting the samples of sine signals in registers.

$$y_i(n) = w_{1,i,x}(n)\sin(w_i n) + w_{2,i,x}(n)\cos(w_i n) \tag{1}$$

The second component, known as the weight computation FxLMS component, is designed for determining the new coefficients in the FxLMS and LMS algorithms.

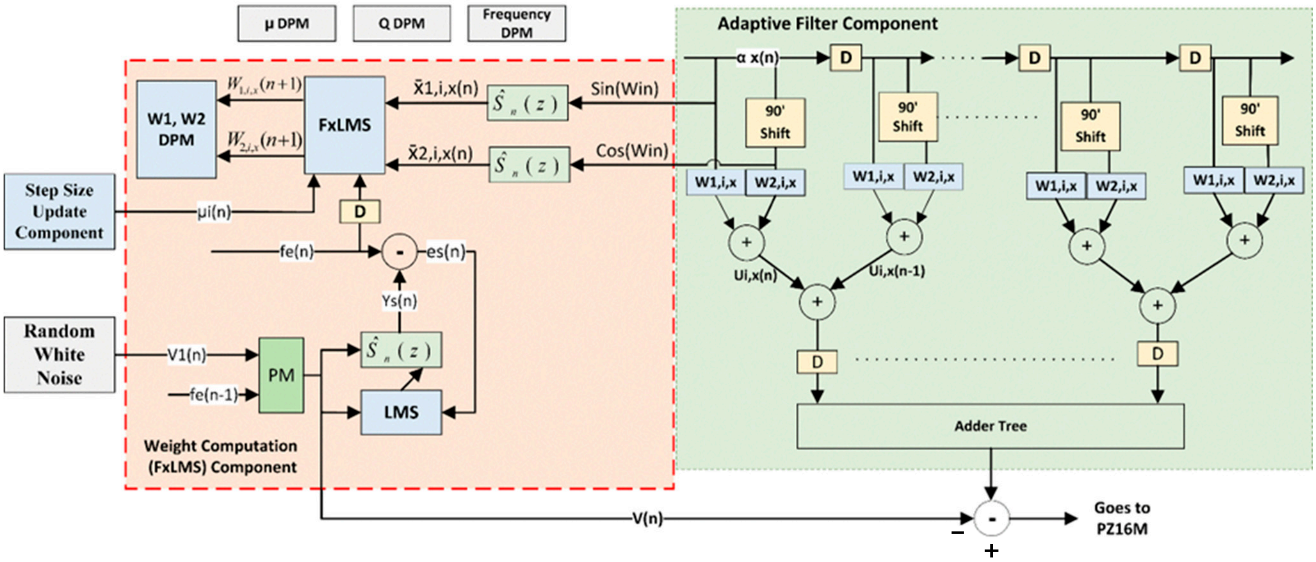

Figure 3. NANC system with four components to identify the microphonics.

The delayed error signal $f_e(n-D)$ (D is a delay), which is the difference between the output of the NANC algorithm $y_i(n)$ and the microphonics measured by the piezo sensor, updates the filter coefficients, $w_{1,i,x}(n+1)$ and $w_{2,i,x}(n+1)$, to minimize the residual error, according to Equations (2)–(5):

$$w_{1,i,x}(n+1) = w_{1,i,x}(n) + \mu_i(n) f_e(n-D)\hat{x}_{1,i,x}(n) \tag{2}$$

$$w_{2,i,x}(n+1) = w_{2,i,x}(n) + \mu_i(n) f_e(n-D)\hat{x}_{2,i,x}(n) \tag{3}$$

$$\hat{x}_{1,i,x}(n) = \sum_{i=1}^{n_w} \hat{s}_i(n)\sin(w_i n) \tag{4}$$

$$\hat{x}_{2,i,x}(n) = \sum_{i=1}^{n_w} \hat{s}_i(n)\cos(w_i n) \tag{5}$$

In the equations, $f_e(n-D)$ is an error signal with a delay, $\mu_i(n)$ is a variable step size, and $\hat{s}_i(n)$ is secondary path modeling in the system.

The third component involves the suggested step-size update component (shown in Figure 4). This component calculates the new variable step size and is responsible for improving the convergence rate, computational complexity, and bit error rate performance of the algorithm over the existing algorithms. To ensure the algorithm's stability and desired steady-state performance, the step size should be constrained to the minimum and maximum values of the step size. Using the comparator and multiplexer creates a simple structure with lower computational complexity.

$$y_s(n) = \sum_{i=1}^{n_w} \hat{s}_i(n) v_1(n-i) f_e(n-i) \tag{6}$$

According to Equation (7), a $\mu_s(n)$ is a variable step size of the SPM, and the coefficients of the transfer function of the actuator are updated by an LMS algorithm. The error signal $f_e(n-i)$ with i delay is used to update the $\hat{s}_i(n+1)$ secondary path coeeficients.

$$\hat{s}_i(n+1) = \hat{s}_i(n) + \mu_s(n) e_s(n) v_1(n-i) f_e(n-i) \tag{7}$$

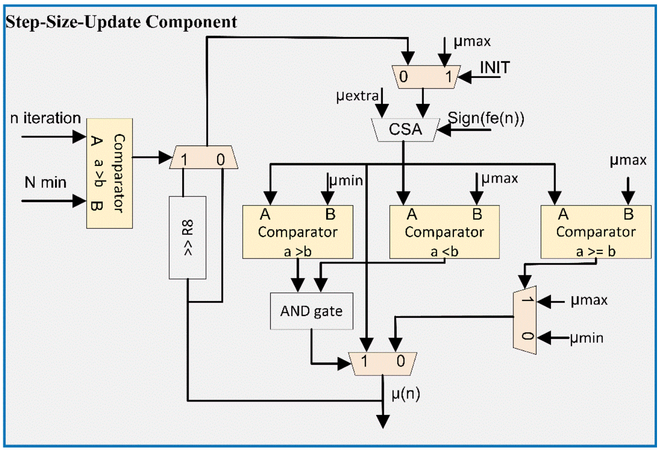

Figure 4. Step-size update component.

The steps of updating the step size of the proposed method are described using Equations (8)–(10):

$$\mu(n+1) = \begin{cases} c * \mu(n) + \mu_{Extra}\mathrm{sign}(e(n)), \; \mu_{min} \le \mu(n) \le \mu_{max} \\ \mu_{max}, \; \mu(n) > \mu_{max} \\ \mu_{min}, \mathrm{Otherwise} \end{cases} \tag{8}$$

$$c = \begin{cases} 2^{-r}, \; i > i'_{min} \\ 1, \; Otherwise \end{cases} \tag{9}$$

$$sign(e(n)) = \begin{cases} +1, \; e(n) > \zeta_{tol} \\ 0, \; |e(n)| < \zeta_{tol} \\ -1, \; e(n) < -\zeta_{tol} \end{cases} \tag{10}$$

where sign(0) is the signum function and ζ_{tol} is a very small positive value that presents the tolerance of the error signal at a steady state. The $\mu_{Extra} > 0$ is a constant value that affects the convergence rate. The proposed method includes two different values to calculate the c parameter; a large c = 1 is taken for the initial iteration. i_{min} is defined as the convergence time of the mean step size, and a small c value is used in the variation process. 2^{-r} is used where r is a positive integer value. Using a hardwired r-bit right shift operation, 2^{-r} can be realized. Better steady-state performance and fewer misadjustments will result from c being extremely close to zero.

According to Equations (8)–(10), when overestimation (measured microphonics < controller output signal) occurs, the sign of e(n) is negative, while the positive sign of e(n) indicates underestimation (measured microphonics > controller output signal). The step size is updated by subtracting a small positive value, μ_{EXTRA}. $\mu(n + 1) = c \times \mu(n) - \mu_{EXTRA}$, whenever overestimation occurs. Similarly, to oppose underestimation, the step size is updated by adding a small positive value, μ_{EXTRA}, $\mu(n + 1) = c \times \mu(n) + \mu_{EXTRA}$, whenever underestimation is encountered [17]. A constant parameter called $\mu_{EXTRA} > 0$ affects both the algorithm's steady-state performance and convergence. The suggested algorithm's steady-state misadjustment equals the prior LMS algorithm structure when c is less than 1.

The final component is responsible for random white noise. It governs the injection or cessation of the white noise in the NANC method. Random white noise component: According to Equation (7), the LMS algorithm needs the random white noise $v_1(n)$ to update the coefficients of the secondary path ($\hat{s}_i(n + 1)$). The performance block is implemented in the NANC method to apply random white noise to the algorithm.

When the error signal converges to the minimum value, the injection of the white noise ($v_1(n)$) will be stopped. Also, the performance block injects white noise into the algorithm when sudden changes happen in the secondary path. Based on the operation of the performance block, the current step-size value is compared to the previous step-size value. If the step size has changes slightly, the random white noise $v_1(n)$ will be stopped. The random white noise will be given back to the algorithm when the error signal is divergent [18].

4. Hardware Implementation

From the results of the earlier tests conducted at the CMTB, it has been observed that the microphone acceleration falls within a range of less than ±5 µg. Consequently, to accurately measure microphonics levels, it becomes imperative to employ an accelerometer with a sensitivity that matches or surpasses this threshold, ideally clocking in at less than ±5 µg. Additionally, our preference leans towards utilizing a digital accelerometer for enhanced precision and reliable data acquisition. Because of these reasons, a solution is suggested to measure and digitize the microphonics: the ADXL355 is a high-performance, low-noise, low drift, and low-power 3-axis MEMS accelerometer developed by Analog Devices. This accelerometer is specifically designed to provide accurate acceleration measurements while consuming minimal power, making it suitable for various applications in industries such as automotive, industrial, aerospace, and consumer electronics. The sensitivity of the accelerometer is 3.9 µg/LSB at ± 2 g. The maximum SPI frequency is 10 MHz; antialiasing filters are provided in the ADXL355 before and after the high-resolution ADC (20 bits). There are user-selectable output data rates (ODR) and filter corners, and the filter's high-pass and low-pass poles can be configured [19]. The ADXL355 can connect to another device with a digital interface (SPI or I^2C). The SPI digital interface is implemented into the vector modulator board (DRTM-VM2) to receive the measured microphonics through the accelerometer. The DRTM-VM2 is constructed as a rear transition module (RTM). The subsystems of the module are management, diagnostic, analog, and digital. Multi-gigabit transceivers (MGTs) are used by the FPGA from the Xilinx Spartan 6 (xc6slx45tfgg484) family to receive data from the control module (AMC). The zone 3 connector's pin assignment complies with DESY's digital class D1.2 standards.

In the deployment of our communication system, as illustrated in Figure 5, we make effective use of RS-485 technology by incorporating ADM3066E integrated circuits on a dedicated transmission board. This strategic approach enhances the efficient transmission of accelerometer data in the form of differential signals. Operating at a data transfer rate of 50 Mbps, our RS-485-based solution not only guarantees reliable communication but also achieves high-speed data transfer over distances of up to 30 m, which is the distance between the location of the cryomodule and the LLRF crate. Harnessing the benefits of RS-485 technology, our system excels in both rapid data transfer and the capability to transmit accelerometer data across extended distances. This makes our solution particularly well-suited for applications that demand long-range communication capabilities. To complement the RS-485 setup, we strategically integrated an Ethernet cable to facilitate the seamless transfer of data from the cryomodule to the LLRF crate. This integration ensures efficient communication within the system, enhancing the overall performance of our communication solution.

On the LLRF crate side, a dedicated transmission board plays a pivotal role in receiving and converting differential signals to single-ended input. These converted signals are directed to the MLVDS buffer (SN65MLVDS204AD), also known as the translator board (SNMLVDS). The translator board serves a crucial function by converting SPI signals to MLVDS signals, which then act as inputs to the RJ45 in the DRTM-VM2 card. Operating under the designation SNMLVDS, the translator board facilitates the conversion of SPI signals to MLVDS format, preparing them for transmission to the DRTM-VM2 card through the RJ45 interface. The utilization of LVDS, with its characteristic differential voltage swing between positive and negative wires, forms the foundation of this differential signaling approach. The voltage difference between these signals not only encrypts the transmitted data but also fortifies the system's resistance to interference from common-mode noise.

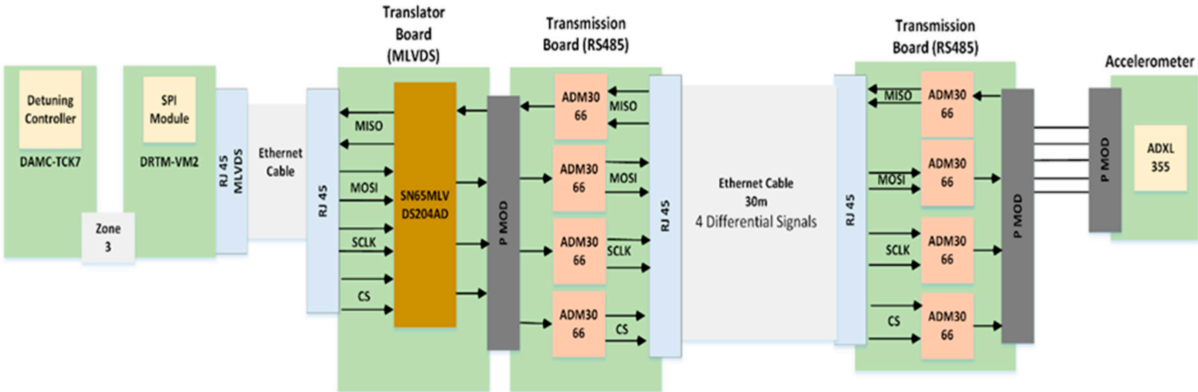

Figure 5. Proposed hardware.

Figure 6 provides a visual representation of the hardware implementation at the CMTB, showcasing (a) the transmission board and the accelerometer on the cryomodule side and (b) the translator and transmission boards on the LLRF crate side. These signals are subsequently transmitted to the DRTM-VM2 card through the RJ45 interface. In Figure 7, the installed hardware is shown at CMTB. Following this transmission, the data processing card (DAMC-TCK7) receives signals from the zone 3 connector and efficiently transfers them to Xilinx Kintex 7 (xc7k420tffg901), thereby completing the data processing workflow. In accordance with the PICMG MTCA.4 specification, the AMC-based Controller (DAMC-TCK7) board was created as a general-purpose high-performance low-latency data processing unit at DESY. The module offers the computational capacity, data storage, communication channels, reference clock, trigger, and interlock signals needed by contemporary LLRF control systems.

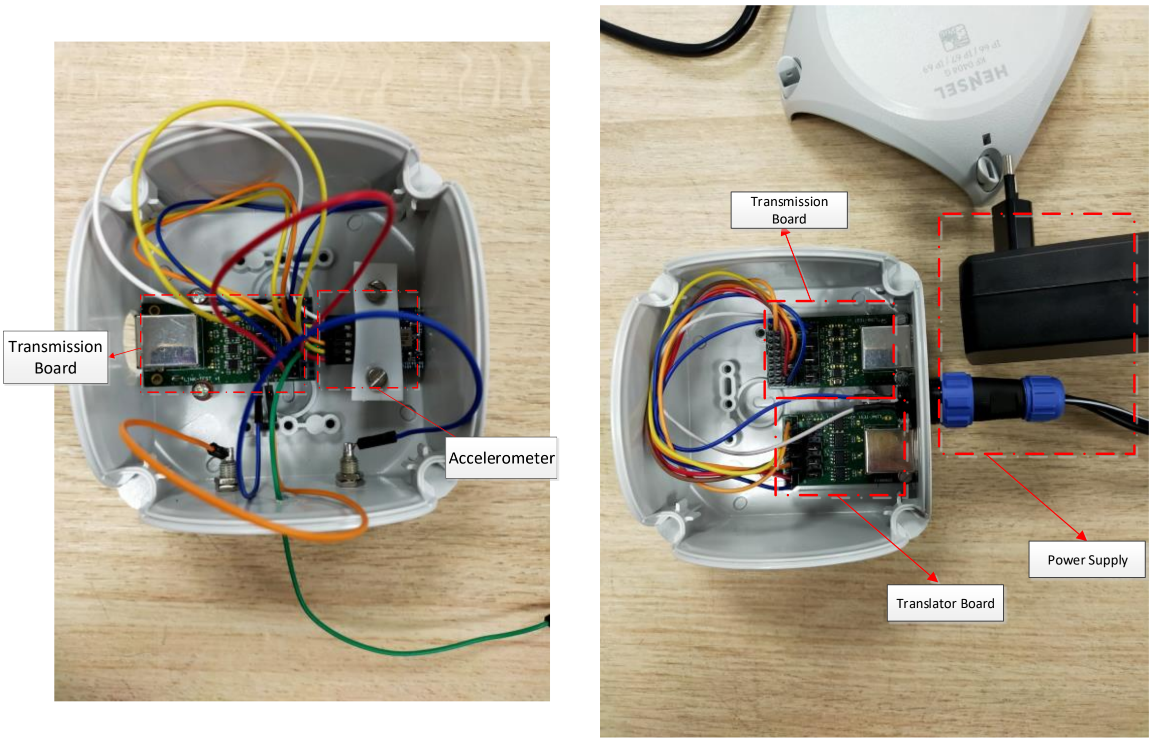

(**a**) (**b**)

Figure 6. Boards for transferring the data from the accelerometer to the LLRF crate. (**a**). Transmission box in Cryomodule side. (**b**). Board box in LLRF crate side.

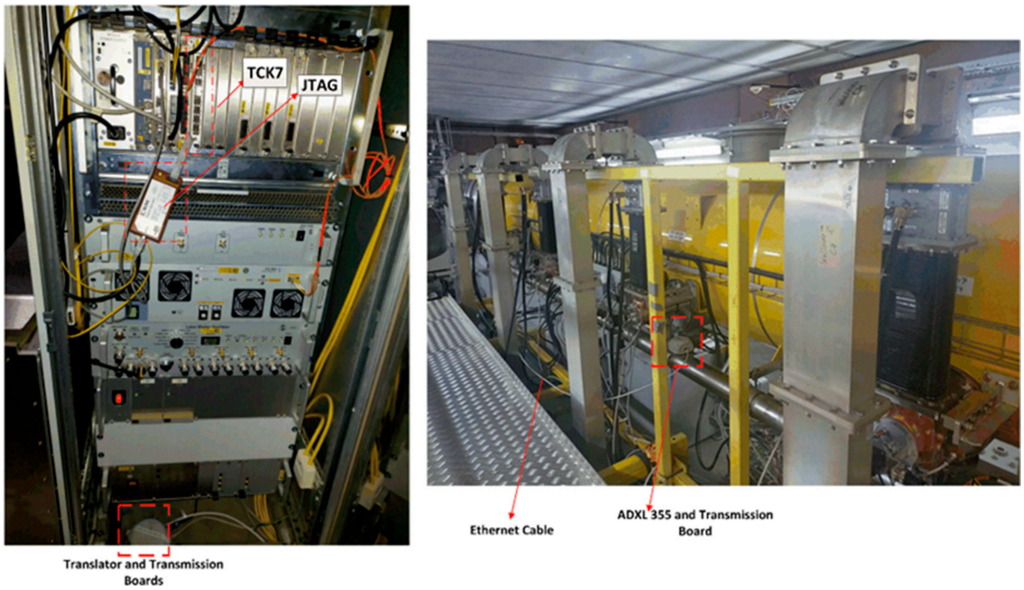

Figure 7. Hardware installed at CMTB.

SPI Interface

The SPI and finite state machine (FSM) configurations are designed to transfer the MOSI (master output and slave input), CS (chip select), and SCLK from the FPGA to the accelerometer and transfer the MISO (master input and slave output, measured microphonics) from the accelerometer to the FPGA. Figure 8 shows the FMS of the top-level module to configure the accelerometer and SPI module. The Mosi signal transfers the configuration options to the accelerometer.

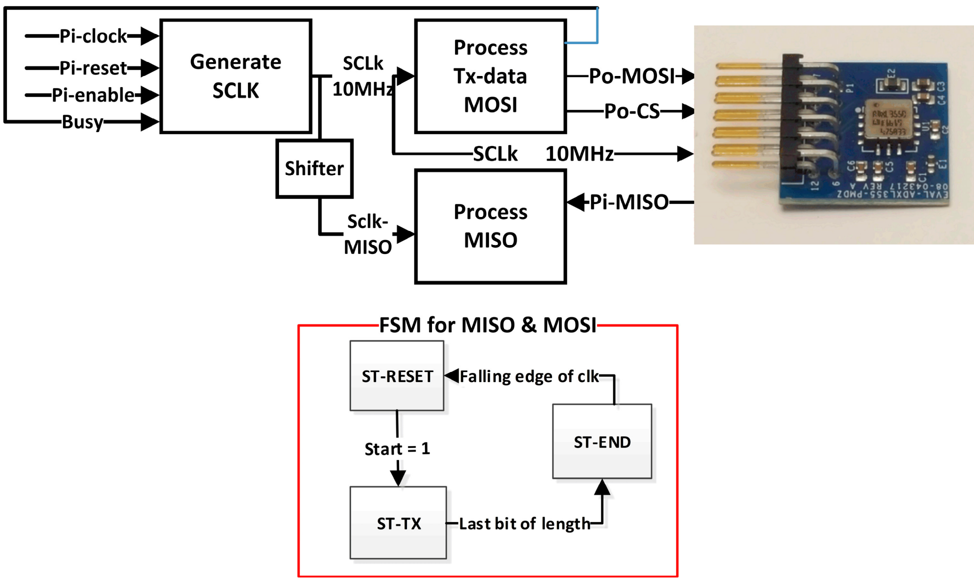

Figure 8. Diagram of the SPI master.

The oscillator generates the clock at 81.25 MHz, and SPI-SCLK is 2 MHz. Some accelerometer features, such as LPF (500 HZ), output data rate (2 KHz), interrupt, reset, and power control, are configured in the SPI module. Based on the datasheet, the data value will be changed from 235 K to 276 K LSB/g. In Figure 9, the accelerometer is mounted on the z-axis, and the chipscope shows the microphonic measured in three axes and SPI signals. In the data processing card, one *sqrt_math* component is implemented to calculate $\sqrt{x^2 + y^2 + z^2}$ of the inputs to the *ENT_FIFO* component.

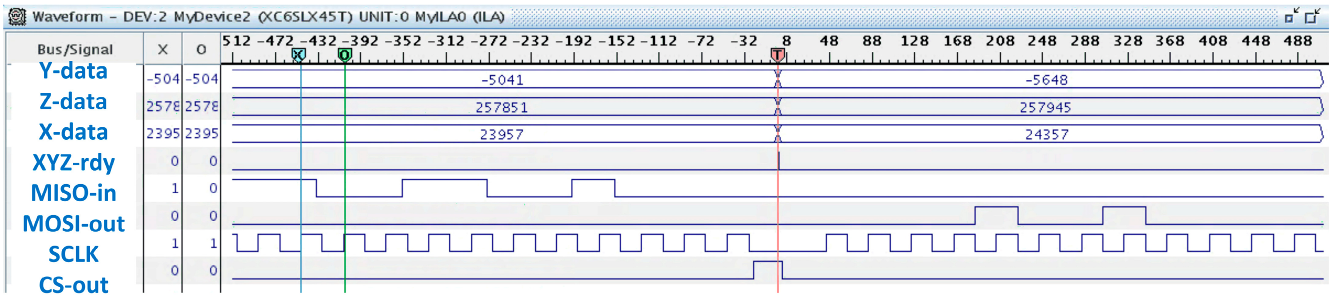

Figure 9. SPI output in the chipscope.

5. Firmware Implementation of the NANC Method

Two adaptive algorithms are used to identify and update the primary coefficients of the FxLMS algorithm and the OSPM filter coefficients through the LMS algorithm. In Figure 10, several FPGA modules are implemented to design the NANC method using HDL language. The measured microphonics are directed to the FIFO module (ENT_FIFO). A hamming window is applied to suppress spurious frequencies caused by discontinuities in the samples and other operations like low-pass filtering. The subsequent FPGA module is the FFT module (fft_ipCore), which converts discrete input signals from the time domain to the frequency domain.

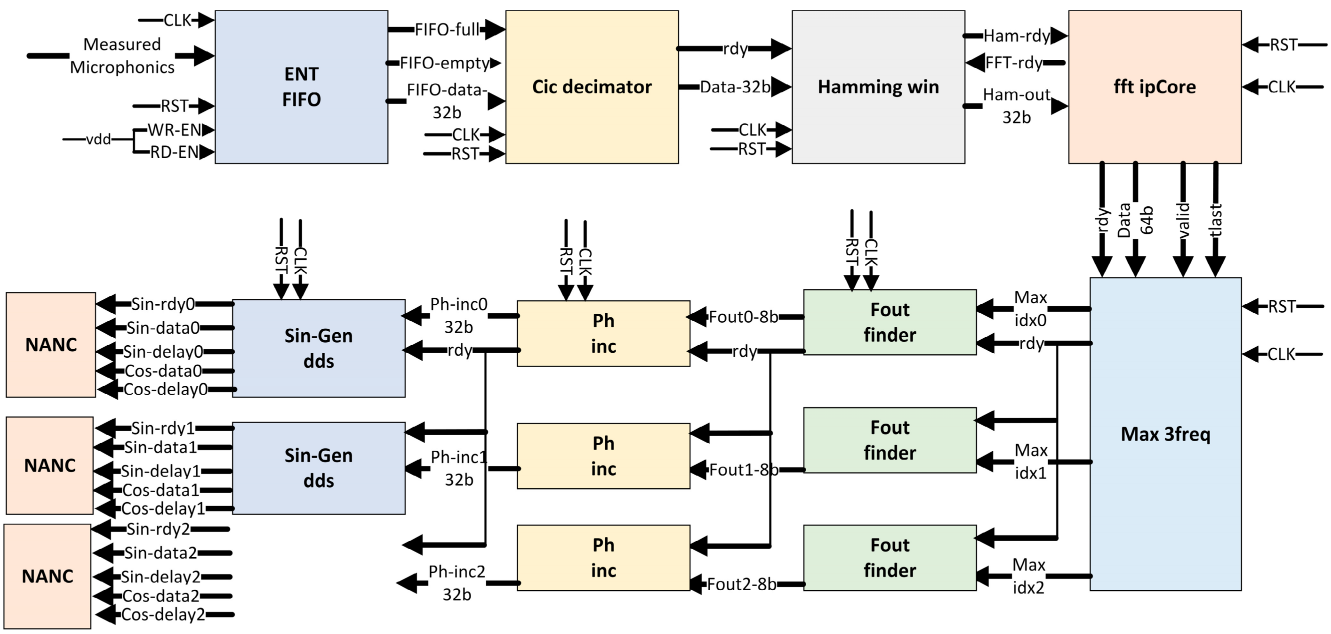

Figure 10. Implementation of the NANC with FPGA modules.

The *max_3freq* module calculates the three highest amplitudes of the microphonics and their corresponding indexes. The *Fout_finder* modules compute the microphonics frequencies based on the indices. The *Ph_inc* module is designed to calculate the phase increment and transmit it to the *Sig_Gen_dds* module, generating sine and cosine signals as input signals to the NANC modules that incorporate the presented NANC method, which is implemented based on the proposed VSS LMS algorithm.

Firmware Implementation Results

The microphonics are measured by the piezo sensor, which is connected to the PZ16M piezo driver module, and a fiber connects the PZ16M to the DAMC-TCK7 card. The software that reads the values from the FPGA and exposes them to Java Data Display (JDDD) is called the piezo server at DESY. The firmware implementation utilized an 18-bit fixed-point operation. Figure 11 shows the measurement setup in the experimental test in the feedforward.

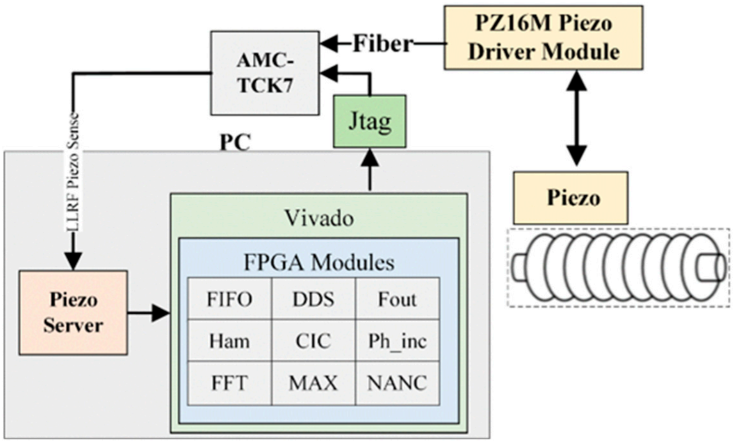

Figure 11. Diagram of the measurement set-up.

Figure 12 displays the microphonics data measured, revealing microphonics occurred at three frequencies with the highest amplitudes at 25 Hz, 28 Hz, and 31 Hz. Figure 13 illustrates the output signals of the FIFO, Hamming Window, and *Fout_finder* modules. The FFT module generates the output (*FFT_tdata*) after a 1024-point process is completed when the *FFT_tlast* goes to '1'. The *Max_3freq* module identifies the three highest-amplitude input signals and their corresponding indices (*Max_IDX0-2*). These identified frequencies (25 Hz, 28 Hz, and 31 Hz) match the frequencies shown in Figure 12. The *Ph_inc* modules calculate the phase increment and send it to the *Sin_Gen_dds* module to generate sine and cosine signals based on the microphonic frequencies.

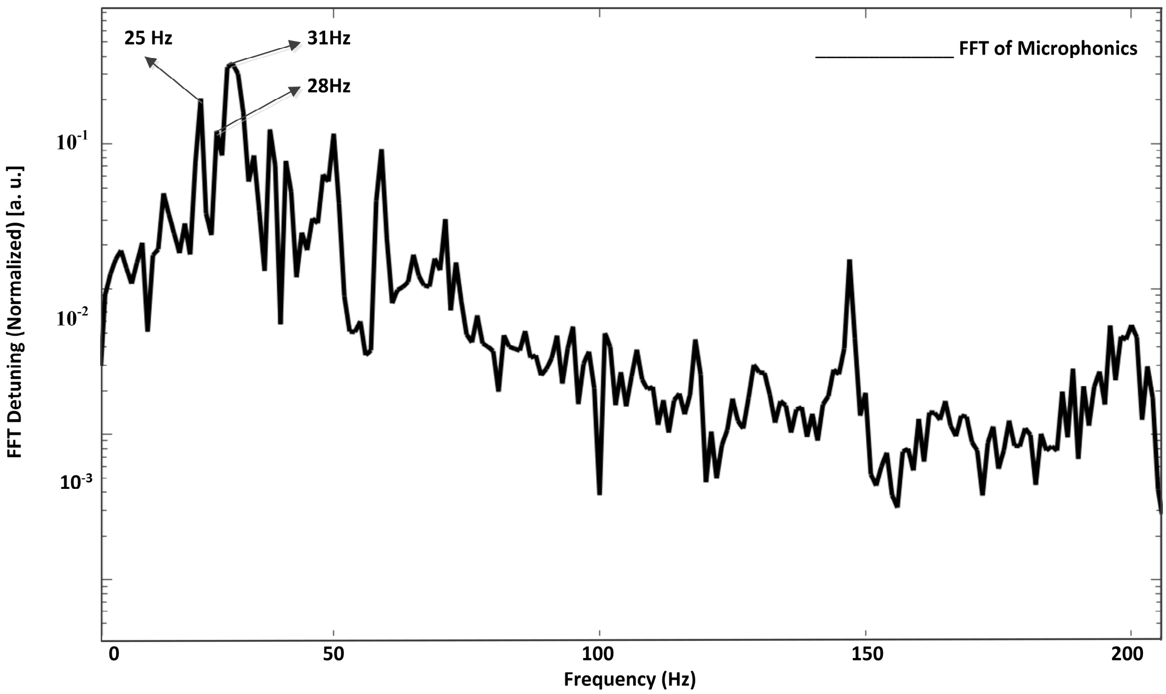

Figure 12. Measured microphonics by piezo sensor.

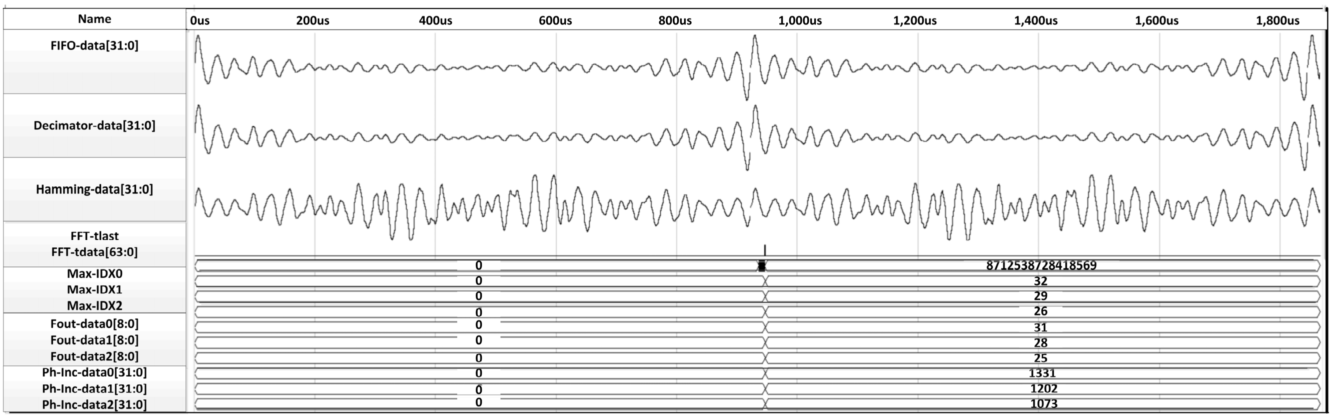

Figure 13. Outputs of the FPGA modules in the NANC method.

In Figure 14, the error signal represents the difference between measured microphonics and the NANC output, convergent to the minimum value. This indicates that the algorithm can efficiently track the microphonics variation with high convergence and tracking ability. The proposed NANC controller is implemented on a DAMC-TCK7 module [20], which features the Xilinx Kintex 7 FPGA with an 81.25 MHz clock cycle. In Table 1, the resource utilization of the implemented architectures is detailed. Referring to the power dissipation report, the power dissipation is as follows: 0.023W for clocks, 0.052W for signals, and 0.034W for DSP, for a total on-chip power of 0.166W.

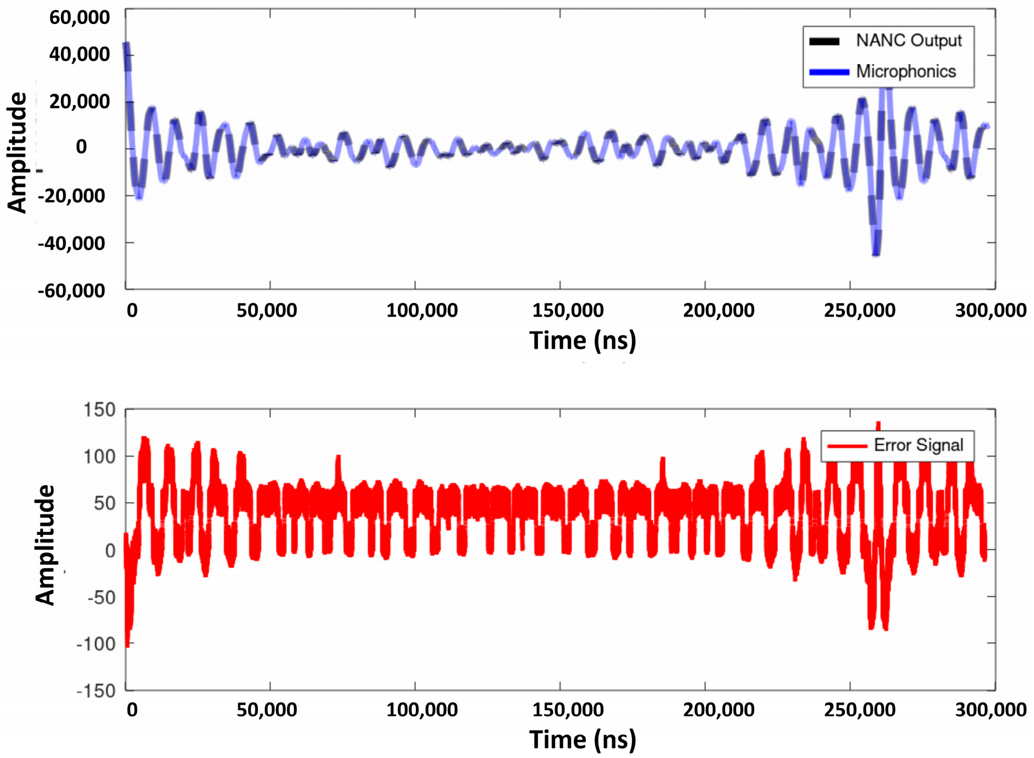

Figure 14. Identification of microphonic changes by the NANC method.

Table 1. Resource utilization on the Xilinx Kintex 7 FPGA.

Module	LUT	FF	DSP	RAM
Available in DAMC-TCK7	260,600	521,200	1680	835
Complete Project	6010	9889	66	30
NANC Module	963	1899	11	0
SPI-Interface Available in DRTM-VM2	296 (81,864)	436 (521,200)	2 (58)	0 (116)

6. Experimental Tests

The microphonics, as measured through the piezo sensor, are visually represented in Figure 15. Notably, microphonics exhibit a consistent oscillation at 49 Hz across the majority of cavities. To optimize the measurement of microphonics at identical frequencies detected by the piezo sensor, an accelerometer is strategically mounted in 30 different locations on the cryomodule. This comprehensive assessment aims to identify the optimal location for capturing microphonics that are compatible with the output of the piezo sensor. The measurements carried out in the Cryomodule Test Bench (CMTB) facility at DESY show vacuum pumps as the main source of microphonics. Based on Table 2, which shows the frequencies with the highest amplitude, the microphonic has the dominant frequencies of approximately 32 Hz and 49 Hz with varying amplitude and phase. Also, slowly varying operating conditions, such as vacuum pumps and helium pressure fluctuations, can cause detuning of the cavities. Given the resonant nature of the cavities at around 49 Hz, the accelerometer is strategically positioned on a pipe proximate to the cavity input. This placement proves effective, as evidenced by the results obtained from Java Data Display (JDDD) analysis, as illustrated in Figure 15. Leveraging the NANC algorithm, compensation for microphonics in multiple cavities becomes possible when the accelerometer successfully detects the 48.024 Hz frequency.

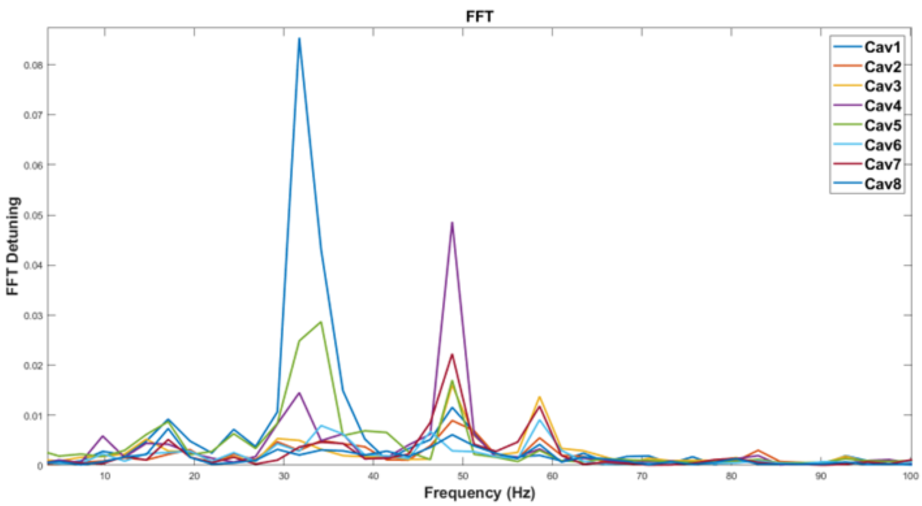

Figure 15. Measured microphonics through the piezo sensor in eight cavities.

Table 2. Resonance frequencies of the microphonics in a cryomodule.

Cavity 1	Cavity 2	Cavity3	Cavity 4	Cavity 5	Cavity 6	Cavity 7	Cavity 8
32	49	49	49	34	59	49	17
49	59	52	32	49	34	59	49
17	34	29	10	17	43	17	59

Figure 16 provides a visual representation of the accelerometer's placement next to the third cavity. Notably, the accelerometer demonstrates its capability to detect frequencies of 48.024 and 72.036 in this optimized configuration. As a result of these findings, the strategically chosen location near the third cavity input proves to be not only optimal for detecting microphonics at the resonant frequency but also extends the accelerometer's capability to capture additional relevant frequencies.

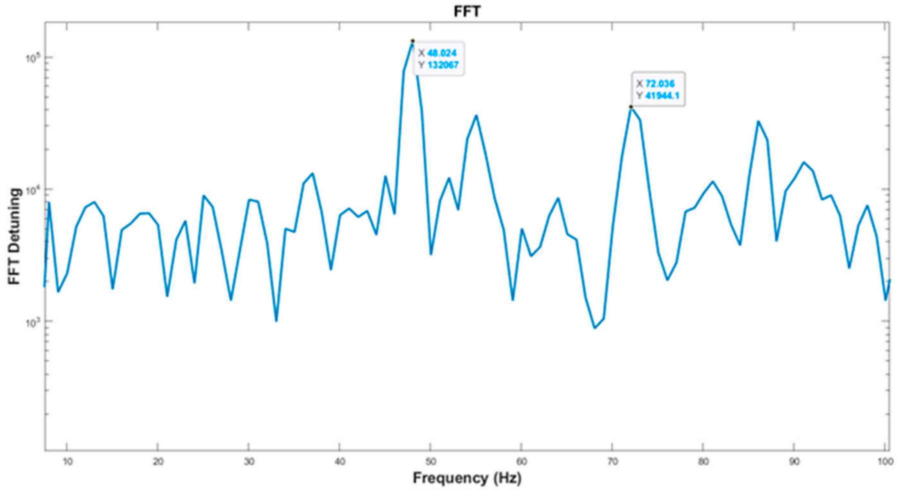

Figure 16. Measure microphonics with an accelerometer at CMTB.

Based on Table 2, Figures 15 and 16, the selected accelerometer can detect the dominant frequency of the microphonics; the proposed method does not need to configure the filter coefficients and the step size manually by the operator. According to the proposed algorithm, there is no need for high FPGA resources to implement it, and it has a high convergence rate.

7. Discussion

In this innovative method, the cumbersome task of manually adjusting microphone frequency and step size with the operator is eliminated. The implementation modules efficiently received the measured microphonic data from the accelerometer. Using the FFT module, the microphonic frequency is accurately calculated, and the DDS module then transfers the generated sinusoidal signals with corresponding microphonic frequencies to the proposed algorithm as input signals.

This methodology introduces a streamlined approach where the proposed algorithm takes charge of identifying and computing filter coefficients based on the microphonic changes. The algorithm ensures a more efficient and accurate adjustment of parameters, enhances tracking ability, and needs fewer FPGA resources due to simple mathematical operations.

In previous DESY research, the piezo sensor inside the cryomodule measured the microphonics. However, in the current approach, an external accelerometer is mounted on the cryomodule to measure the microphonics. Due to the uncorrelation between the measured microphonics by the external accelerometer and the microphonics inside the cryomodule, an advanced algorithm becomes imperative in this proposed methodology.

However, it is important to note a limitation of the implemented method, which involves the use of a single accelerometer. This constraint arises due to the necessity of transferring data from RJ45 to DRTM-VM2. Consequently, the implementation requires four inputs and outputs for transmitting an SPI protocol. Despite this limitation, the overall efficiency and precision achieved by the proposed algorithm underscore its potential for advancing the field of microphone compensation.

8. Conclusions

The microphonics changes on the cryomodule restrict the performance of the PI controller at the LLRF system. Therefore, the proposed NANC method is implemented based on the presented VSS LMS algorithm to compensate for the microphonics effects on the cryomodule. Some advantages of the proposed method are:

1. There is no need to identify the transfer function of the cryomodule and plant.
2. Low computational complexity.
3. High tracking ability.

The proposed method identified three frequencies of the microphonics with the highest amplitude. In principle, the adaptive filter coefficients of the NANC method are adjusted during the operation of the system by an iterative optimization method. The presented method is implemented on the MicroTCA boards (DAMC-TCK7 and DRTM-VM2 cards) and permits control of the microphonics changes in CW mode. A microelectromechanical systems (MEMS) accelerometer is mounted on several locations of the cryomodule at CMTB, and the optimal location is on the pipe near the cavity input for measuring the microphonic (mechanical) vibration. The component implementation is integrated into the LLRF controller module to compensate for the measured microphonics changes. In the next step of the project, the microphonic module will be extended in piezo feedback in the DESY firmware and receive the probe phase and forward phase as the inputs of the microphonics module to identify the filter coefficients based on the microphonics changes.

Author Contributions: Conceptualization, F.A., W.C., W.J., Ł.B., J.B., A.B. and G.J.; methodology, F.A., W.J., W.C. and Ł.B.; software, F.A.; validation, F.A., W.J. and Ł.B.; formal analysis, F.A.; investigation, F.A.; writing—original and draft preparation, F.A.; writing—review and editing, F.A., W.C., W.J., J.B. and G.J.; supervision, W.C. All authors have read and agreed to the published version of the manuscript.

Funding: This project has been realized at Lodz University of Technology in Lodz, Poland, and DESY in Hamburg, Germany.

Data Availability Statement: Derived data supporting the findings of this study are available from the corresponding author on request.

Acknowledgments: This work (FPGA-Based Implementation of Adaptive Noise Controller for Continuous Wave Superconducting Cavity) was completed while the first author (Fatemeh Abdi) was at the Interdisciplinary Doctoral School at Lodz University of Technology, Poland.

Conflicts of Interest: The authors declare no conflict of interest.

References

1. DESY. Hamburg. FLASH-The Free-Electron Laser in Hamburg. Available online: https://flash.desy.de/ (accessed on 25 October 2023).
2. Brinkmann, R. *XFEL: The European X-ray Free-Electron Laser-Technical Design Report*; DESY: Hamburg, Germany, 2007. Available online: https://bib-pubdb1.desy.de/record/77248/files/european-xfel-tdr.pdf (accessed on 25 October 2023).
3. Przygoda, K. Development of a Control System for Fast Frequency Tuners of Superconducting Resonant Cavities for FLASH and XFEL Experiments. Ph.D. Thesis, Politechnikac Łódzka, Łódz, Poland, 2011.
4. Cichalewski, W.; Sekutowicz, J.; Napieralski, A.; Rybaniec, R.; Branlard, J.; Ayvazyan, V. Continuous Wave Operation of Superconducting Accelerating Cavities with High Loaded Quality Factor. *IEEE Trans. Nucl. Sci.* **2020**, *67*, 2119–2127. [CrossRef]
5. Bellandi, A.; Branlard, J.; Cruz, J.D.; Aderhold, S.; Benwell, A.; Brachmann, A.; Hoobler, S.; Ratti, A.; Gonnella, D.; Nelson, J.; et al. Narrow bandwidth active noise control for microphonics rejection in superconducting cavities at LCLS-II. *arXiv* **2022**, arXiv:2209.13896.
6. Leewe, R.; Shahriari, Z.; Moallem, M. Resonance frequency control of RF normal conducting cavity using gradient estimator of reflected power. *Nucl. Instrum. Methods Phys. Res. Sect. A Accel. Spectrometers Detect. Assoc. Equip.* **2017**, *869*, 172–179. [CrossRef]
7. Banerjee, N.; Hoffstaetter, G.; Liepe, M.; Quigley, P.; Zhou, Z. Active suppression of microphonics detuning in high QL cavities. *Phys. Rev. Accel. Beams* **2019**, *22*, 2–9. [CrossRef]
8. Kang, H.S. Achievement and prospect of the PAL-XFEL. *J. Korean Phys. Soc.* **2022**, *80*, 684–692. [CrossRef]
9. Farhang-Boroujeny, B. *Adaptive Filters: Theory and Applications*; John Wiley & Sons: Hoboken, NJ, USA, 2013.

10. Kuntzsch, M.; Steinbrück, R.; Schurig, R.; Hierholzer, M.; Killenberg, M.; Schmidt, C.; Hoffmann, M.; Iatrou, C.; Rahm, J.; Rutkowski, I. MicroTCA.4-based LLRF for CW Operation at Elbe-Status and Outlook. In Proceedings of the 6th International Beam Instrumentation Conference, Grand Rapids, MI, USA, 20–24 August 2017; pp. 101–103.
11. Tamura, F.; Sugiyama, Y.; Yoshii, M.; Yamamoto, M.; Okita, H.; Ohmori, C.; Nomura, M.; Shimada, T.; Hasegawa, K.; Hara, K.; et al. Commissioning of the next-generation LLRF control system for the Rapid Cycling Synchrotron of the Japan Proton Accelerator Research Complex. *Nucl. Instrum. Methods Phys. Res. Sect. A Accel. Spectrometers Detect. Assoc. Equip.* **2021**, *999*, 165211. [CrossRef]
12. Li, H.C.; Tsai, H.H.; Lin, T.F.; Chiou, W.S.; Chang, S.H.; Hsiao, F.Z.; Liao, W.R.; Chuang, P.S.D. Redundant Compressor System for the Helium Cryogenic Plant at TPS. *IOP Conf. Ser. Mater. Sci. Eng.* **2017**, *171*, 12041. [CrossRef]
13. Elliott, S.; Darlington, P. Adaptive cancellation of periodic, synchronously sampled interference. *IEEE Trans. Acoust. Speech Signal Process.* **1985**, *33*, 715–717. [CrossRef]
14. Chaplin, B. The Cancellation of Repetitive Noise and Vibration. In Proceedings of the INTER-NOISE and NOISE-CON Congress and Conference, Miami, FL, USA, 8–10 December 1980; pp. 507–958.
15. Widrow, B.; Glover, J.R.; McCool, J.M.; Kaunitz, J.; Williams, C.S.; Hearn, R.H.; Zeidler, J.R.; Dong, J.E.; Goodlin, R.C. Adaptive noise cancelling: Principles and applications. *Proc. IEEE* **1975**, *63*, 1692–1716. [CrossRef]
16. Ziegler, E., Jr. Selective Active Cancellation System for Repetitive Phenomena. U.S. Patent 4 878 188, 17 September 1992.
17. Bose, S.D.A.; Chakrabarti, I. Framework for automated earthquake event detection based on denoising by adaptive filter. *IEEE Trans. Circuits Syst. I Regul. Pap.* **2020**, *67*, 3070–3083. [CrossRef]
18. Li, H.; Tian, H. A New VSS-LMS Adaptive Filtering Algorithm and Its Application in Adaptive Noise Jamming Cancellation System. In Proceedings of the IEEE Circuits and Systems International Conference on Testing and Diagnosis, Chengdu, China, 28–29 April 2009; pp. 1–4.
19. Data Sheet, Low Noise, Low Drift, Low Power, 3-Axis MEMS Accelerometers, ADXL354/ADXL355. Available online: https://www.analog.com/media/en/technical-documentation/data-sheets/adxl354_355.pdf (accessed on 25 October 2023).
20. SIS8300-KU MTCA.4 DIGITIZER, 10 Channel 125 MS/s 16-Bit with Fast Feedback DACs. Available online: https://www.struck.de/sis8300-ku.html (accessed on 25 October 2023).